ChemComm

COMMUNICATION

View Article Online
View Journal | View Issue

Cite this: *Chem. Commun.*, 2021, **57**, 3571

Received 8th December 2020,
Accepted 15th February 2021

DOI: 10.1039/d0cc07974j

rsc.li/chemcomm

Isomer of linker for NU-1000 yields a new *she*-type, catalytic, and hierarchically porous, Zr-based metal–organic framework†

Zhiyong Lu, *[ab] Rui Wang,[b] Yijun Liao,[b] Omar K. Farha,[b] Wentuan Bi,[bc] Thomas R. Sheridan,[b] Kun Zhang,[bd] Jiaxin Duan,[b] Jian Liu[b] and Joseph T. Hupp*[b]

The well-known MOF (metal–organic framework) linker tetrakis (p-benzoate)pyrene ($TBAPy^{4-}$) lacks steric hindrance between its benzoates. Changing the 1,3,6,8-siting of benzoates in $TBAPy^{4-}$ to 4,5,9,10-siting introduces substantial steric hindrance and, in turn, enables the synthesis of a new hierarchically porous, *she*-type MOF $Zr_6(\mu_3\text{-}O)_4(\mu_3\text{-}OH)_4(C_6H_5COO)_3(COO)_3(TBAPy\text{-}2)_{3/2}$ (NU-601), where $TBAPy\text{-}2^{4-}$ is the 4,5,9,10 isomer of $TBAPy^{4-}$. NU-601 shows high catalytic activity for degradative hydrolysis of a simulant for G-type fluoro-phosphorus nerve agents.

Metal–organic frameworks (MOFs) have shown promise for applications in gas storage and separations, chemical sensing, and catalysis.[1–4] For heterogeneous catalysis, MOFs with hierarchical porosity (*i.e.*, interconnected pores of differing size) are often favoured over those offering pores of only a single size.[5–8] Thus, micropores, and associated molecular confinement, can be advantageous for catalytic selectivity, while mesopores can facilitate efficient mass transport[9] – the ''highways and byways'' of molecular-scale porosity. Or, mesopores can serve to host larger biological moieties like enzymes, with interconnected micropores size-excluding these same species and thereby providing routes for delivering substrates and removing products.[10–12]

Among the most promising as heterogeneous catalysts and as catalyst supports are chemically and thermally robust, zirconium-based MOFs.[13–17] Prominent within the group offering hierarchical porosity are ***csq***-type Zr-MOFs (exemplified by PCN-222/MOF-545,[11,13] NU-1000,[10] and their many reticular expansions). Beyond those with ***csq*** topology, however, the number and variety of Zr-MOFs presenting interconnected hierarchical channel structures,[18] are few.

Herein, we present a new way of obtaining hierarchical channels structures, exemplified by a new ***she***-type Zr-MOF, **NU-601**.‡ Briefly, shifting the positions of benzoates in the linker $TBAPy^{4-}$ (1,3,6,8-tetrakis(*p*-benzoate)pyrene^{4-}) from the 1,3,6, and 8 carbons of pyrene to 4,5,9, and 10, amplifies ring steric interactions, increases benzoate/pyrene dihedral angles, and facilitates the formation of hierarchically porous **NU-601**, with formula $Zr_6(\mu_3\text{-}O)_4(\mu_3\text{-}OH)_4(C_6H_5COO)_3(HCOO)_3(TBAPy\text{-}2)_{3/2}$, where formate and benzoate are displaceable, nonstructural ligands. Notably, the activated, water-equilibrated version of **NU-601** (a 6-connected MOF) exhibits higher catalytic activity than 8-connected NU-1000 for hydrolytic degradation of nerve agent simulants.

In the synthesis of Zr-MOFs, variations in linker structure and auxiliary ligand structure (remnent synthesis modulators), rather than node structure, tend to provide structural diversity, as the majority feature the same $Zr_6(\mu_3\text{-}O)_4(\mu_3\text{-}OH)_4$ node. For tetratopic carboxylate linkers, differences in symmetry and in the geometry of the connections to inorganic nodes lead to differences in MOF topology. Taking the linker tetrakis(4-carboxyphenyl)-porphyrin (TCPP) in Scheme 1 as an example, a TCPP linker with C_{2h} symmetry will lead to the ***scu***-type NU-902,[19] but a small variation of the torsion angle between the terminal benzene ring and the central porphyrin ring leads to the ***shp***-type PCN-223 (Fig. S12, ESI†).[20] When the linker's configuration possesses C_{2v} symmetry, the torsion angle φ_{cc} between the central plane (green plane in Scheme 1) and the terminal carboxylic plane (blue in Scheme 1) drives the topology toward either ***csq*** or ***she***. As illustrated in Scheme 1, when φ_{cc} is close to or less than 60°, the overall dihedral angle between adjacent linker would be 120°, leads to a ***csq***-type MOF.[11] If φ_{cc} is larger (about 80°), adjacent linkers will be

[a] *College of Mechanics and Materials, Hohai University, Nanjing 210098, China. E-mail: johnlook1987@gmail.com*
[b] *Department of Chemistry, Northwestern University, 2145 Sheridan Road, Evanston, Illinois 60208, USA. E-mail: j-hupp@northwestern.edu*
[c] *Department of Chemistry, University of Science and Technology of China, Hefei 230026, China*
[d] *School of Chemical Engineering, Nanjing University of Science & Technology, Nanjing 210094, China*

† Electronic supplementary information (ESI) available: Details of synthesis, single-crystal data, PXRD, ^{31}P NMR spectra. CCDC 2015123 and 2015124. For ESI and crystallographic data in CIF or other electronic format see DOI: 10.1039/d0cc07974j

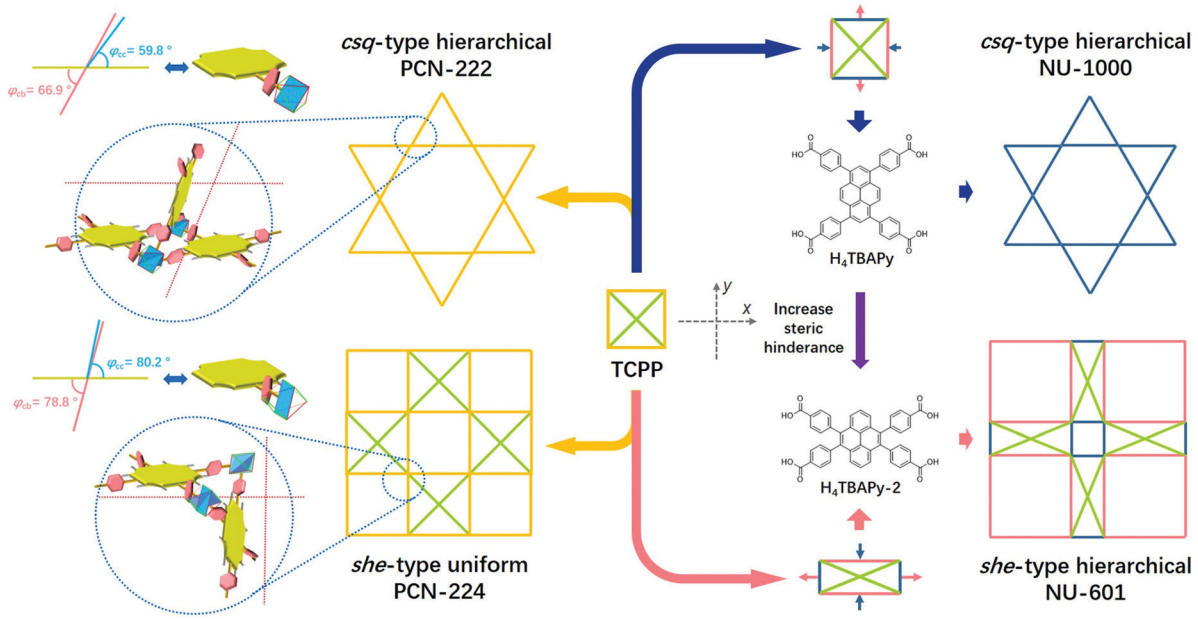

Scheme 1 Illustration of linker geometries and configurations leading to hierarchical Zr-MOFs with different topologies.

nearly perpendicular, which leads to the ***she***-type net.[21] This angle is largely correlated with the torsion angle φ_{cb} between the central plane and the plane of the terminal benzene ring (blue in Scheme 1). When φ_{cb} is sufficiently small (less than 60°), φ_{cc} is less likely to exceed 80°, which disfavours an ***she***-net. In TCPP, benzene rings are partially hindered by neighbouring pyrrole rings, thus φ_{cb} always exceeds 60°. However, for the linkers of NU-1000,[10] PCN-128,[22] and PCN-608-OH,[12] due to conjugation between the linker and peripheral benzenes, φ_{cb} in every case has been less than 60° (Table S2, ESI†), and thus, no ***she***-type MOFs utilizing these linkers have been synthesized until now.

Due to the conjugation in H_4TBAPy, φ_{cc} in H_4TBAPy is sufficiently small to form a hierarchical ***csq***-type net, **NU-1000**. Meanwhile, although H_4TBAPy exhibits lower symmetry than TCPP, the widths of both *meso*- and micro-pores are solely dependent on the length of one edge of the planar linker, as shown in Scheme 1 by the edge parallel to the *x* axis. However, for ***she***-type Zr-MOFs, the pore size is dependent on both edge lengths of a nominally rectangular linker, and so unequal lengths along *x* and *y* axes are anticipated to yield orthogonal hierarchal channels. A pyrene core could still be used to introduce different edge lengths to obtain an ***she***-type Zr-MOF, but alteration of the linker structure would be necessary. To avoid forming ***csq***-type structures, φ_{cc} could be altered – for example, by relocating benzene rings and engendering steric interference between them. As shown in Scheme 1, this can be accomplished, and unequal edge lengths can be created, by replacing $TBAPy^{4-}$ with TBAPy-2^{4-}, an isomer featuring *p*-benzoate substituents at the 4, 5, 9, and 10 carbons of pyrene.

With the isomer in hand, the desired new ***she***-type MOF, **NU-601**, proved straightforward to obtain in phase-pure, single-crystal form. Solvothermal reaction of H_4TBAPy-2 with $ZrOCl_2{\cdot}8H_2O$ in *N*,*N*-dimethylformamide (DMF) in the presence of benzoic acid as a modulator produced colourless cubic crystals, $Zr_6(\mu_3\text{-}O)_4(\mu_3\text{-}OH)_4(C_6H_5COO)_3(HCOO)_3(TBAPy\text{-}2)_{3/2}$ (**NU-601-as-syn**). To remove the modulators, **NU-601-as-syn** was heated in 8 M aq. HCl in DMF overnight at 100 °C, yielding **NU-601-activated**. **NU-601** in microcrystalline powder form (**NU-601-p**) was synthesized by the solvothermal reaction of H_4TBAPy-2 with $ZrCl_4$ in *N*,*N*-diethylformamide (DEF) in the presence of formic acid as a modulator. By controlling the reaction time and the concentration of formic acid, crystallites of ~1 μm, ~5 μm, or ~10 μm (designated **NU-601-1 μm**, **NU-601-5 μm**, or **NU-601-10 μm**) can be created.

Single-crystal X-ray structure analysis revealed that **NU-601-as-syn** crystallizes in the cubic space group $Pm\bar{3}m$, with $a = b = c = 34.8374(5)$ Å. This new MOF contains Zr_6 nodes and TBAPy-2 linkers in a 2 : 3 ratio. Each Zr_6 cluster consists of two kinds of crystallographically independent Zr atoms (Zr1 and Zr2) and eight μ_3-O/OH entities. Each cluster ligates three nonstructural formates, and three nonstructural benzoates, and is connected to six TBAPy-2 linkers. Zr1 is eight-coordinated by two O atoms from carboxylates of two different TBAPy-2 linkers, four μ_3-O/OH entities, and two O atoms of two different formates. Zr2 is also eight-coordinated by two O atoms from carboxylates of two different TBAPy-2 linkers and four μ_3-O/OH entities, but is coordinated by two O atoms of two different benzoates (Fig. 1a). Three Zr1 and three Zr2 atoms are connected by eight μ_3-O/OH atoms, forming a Zr_6O_8 cluster with C_{3v} symmetry, which makes further connections *via* six TBAPy-2 linkers. The space group of **NU-601-activated** remains $Pm\bar{3}m$, with unit cell parameters of $a = b = c = 35.081(15)$ Å. However, the nonstructural benzoate ligands were successfully removed from **NU-601-as-syn** and no obvious formate could be assigned in the crystal structure, likely due to severe local disorder. Therefore, all the coordinated terminal oxygen atoms were assigned as terminal H_2O/OH entities, although evidence for three labile formates per Zr_6 node could be found in the ^{1}H NMR spectra of base-digested **NU-601-activated** (Fig. S7, ESI†). In both **NU-601-as-syn** and **NU-601-activated**, the rings

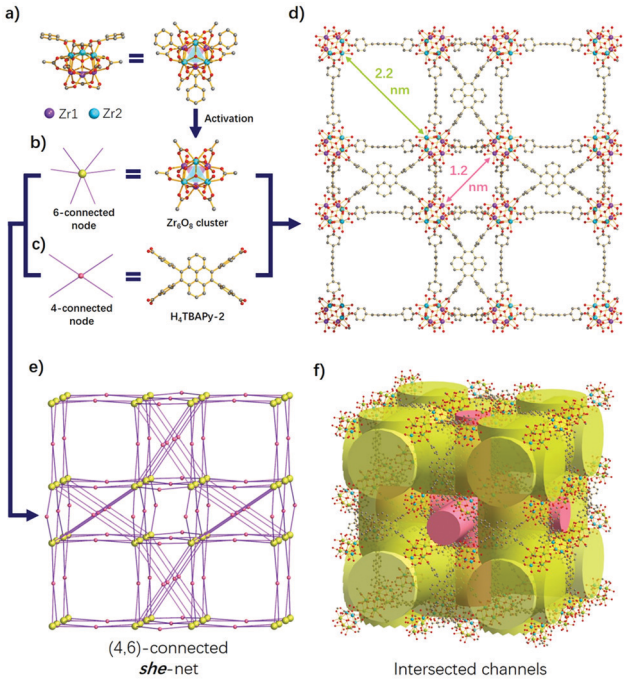

Fig. 1 (a) The coordination environment of Zr_6 node; (b) and (c) are the simplification of Zr_6 node and TBAPy-2, respectively; (d) micro- and meso-channels in **NU-601**; (e) topology of **NU-601**; (f) intersected channels in **NU-601**.

comprising each pair of benzenes in TBAPy-2 are in close proximity, but are unable to conjugate with the pyrene core. Instead, due to their mutual steric interference, they are nearly perpendicular to pyrene, with a torsion angle of 85°. In turn, φ_{cc} is *ca.* 82°, which gives rise to a (4,6)-connected ***she***-net with the point symbol $\{4^4{\cdot}6^2\}_3\{4^6{\cdot}6^6{\cdot}8^3\}_2$, where each TBAPy-2 is simplified as a 4-connected node and each Zr_6O_8 simplified as a 6-connected node (Fig. 1b, c and e).

The difference in edge length of TBAPy-2 along the *x* and *y* directions, as shown in Scheme 1, leads to the hierarchical channels in **NU-601** (Fig. 1d and f). The channel widths are 2.2 and 1.2 nm. Each type of channel is intersectional with itself and is separated by linkers, as shown in Fig. 1f. The solvent-accessible volume, as estimated by PLATON, is 76%.

The permanent porosity of **NU-601-activated** was analysed based on N_2 sorption at 77 K. As shown in Fig. 2a, the N_2 adsorption for **NU-601-activated** exhibits a reversible type IVb isotherm with a plateau starting at $P/P_0 \approx 0.2$. This type of isotherm is typical for MOFs that present both micro- and mesopores. The limiting N_2 uptake by **NU-601-activated** is 510 $cm^3\ g^{-1}$. The BET (Brunauer–Emmer–Teller) surface area of **NU-601-activated** is 1130 $m^2\ g^{-1}$. NL-DFT-analysed pore-size distributions indicate pore diameters of *ca.* 13 and 23 Å, consistent with the single-crystal structure.

Zr-MOFs have been widely explored for catalytic hydrolytic detoxification of organophosphate-based nerve agents and their simulants.[23–26] Minimum requirements for catalytic activity include Lewis acidic sites (such as Zr(IV)) that can activate hydrolysis targets *via* target displacement of labile ligands such

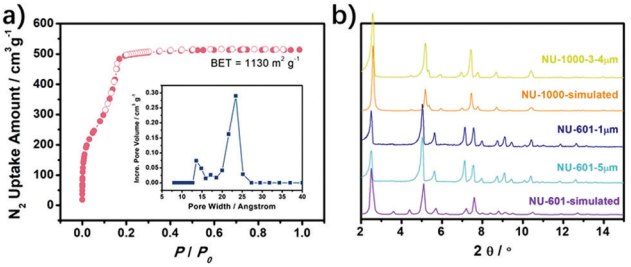

Fig. 2 (a) N_2 adsorption isotherm and pore size distribution (inserted) of **NU-601-Activated**; (b) PXRD patterns of **NU-601** and **NU-1000**.

as H_2O. In studies that admittedly are limited, relative activities of various Zr-MOFs increase with increasing numbers of reactant-accessible Zr(IV) sites – but by amounts that are far greater than anticipated based solely on differing numbers of sites. In any case, **NU-601** (6-connected) presents more candidate Lewis acid sites (6) than does either NU-1000 (8-connected Zr_6 node; 4 potential active-sites)[27] or UiO-66 (nominally 12-connected; *ca.* 0–2 active sites).[28,29]

Therefore, we tested the catalytic performance of **NU-601** for the hydrolysis of dimethyl 4-nitrophenyl phosphonate (DMNP), a simulant for G-type fluoro-phosphorus nerve agents such as sarin. The activity was assessed with 6 mol% of the MOF/catalyst, and the DMNP conversion was monitored by *in situ* ^{31}P NMR. As shown in Fig. 3 and Table S3 (ESI†), the initial reaction half-life is about 5 min (**NU-601-5 μm**), with conversion reaching 90% after 30 min, which is substantially faster than observed with NU-1000 samples featuring similar particle size (3–4 μm, half-life $t_{1/2}$ = 11 min).[27,30] As both MOFs possess hierarchical porosity, we must look elsewhere to understand

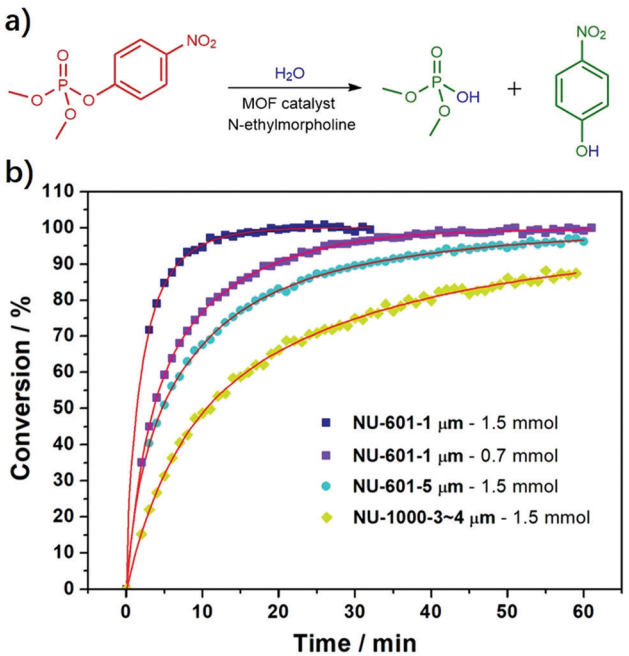

Fig. 3 (a) Hydrolysis reaction of DMNP. (b) Hydrolysis profiles of DMNP with **NU-601** and **NU-1000**.

the difference in catalytic activity. We suggest that the activity advantage for **NU-601** is related to: (a) the aforementioned difference in node-linker connectivity and its effect upon the number and potential strength of Lewis acid sites, and (2) faster substrate transport by isotropic (3D) diffusion in **NU-601** compared with predominantly anisotropic (1D) diffusion in NU-1000. Consistent with a rate-constraining role for substrate transport, replacing **NU-601-5 μm** with **NU-601-1 μm** pushes the half-life for catalytic hydrolysis of DMNP to below 2 min. Reducing the loading of **NU-601-1 μm** to 3 mol%, increases the reaction half-life to 3.5 min and yields an initial "per node" turnover frequency of 0.085 s^{-1}. The high catalytic reactivity suggests that **NU-601** is a good candidate for efficiently detoxifying real nerve agents.

In summary, we obtained a new hierarchically porous ***she***-type Zr-MOF, **NU-601**, by replacing the linker $TBAPy^{4-}$, from NU-1000, with a sterically congested isomer, TBAPy-2^{4-}. The 6-connected nodes and overall 3D mesoporosity of **NU-601** endow it with high catalytic activity for degradative hydrolysis of a simulant of G-type nerve agents. This study provides insight into creating hierarchically porous MOFs for heterogeneous catalysis. We hope to capitalize on this new approach in ongoing studies of intra-MOF molecular-transport and heterogeneous catalysis.

This work was supported as part of the Inorganometallic Catalyst Design Center, an EFRC funded by the U.S. Department of Energy (DOE), Office of Science, Office of Basic Energy Sciences (DE-SC0012702). For work specifically on catalytic hydrolysis of nerve-agent simulants we gratefully acknowledge DTRA (grant HDTRA1-18-1-0003). Z. L. gratefully acknowledges support from the National Natural Science Foundation of China (21601047), the Fundamental Research Funds for the Central Universities (2018B17614), and the China Scholarship Council (CSC) (201806715039).

Conflicts of interest

There are no conflicts to declare.

Notes and references

‡ MOFkey:[31] Zr. MWVMNBLQHRBBOY. MOFkey-v1.she (**NU-601**).

1 R.-B. Lin, S. Xiang, H. Xing, W. Zhou and B. Chen, *Coord. Chem. Rev.*, 2019, **378**, 87–103.
2 P. Wu, Y. Li, J. J. Zheng, N. Hosono, K. I. Otake, J. Wang, Y. Liu, L. Xia, M. Jiang, S. Sakaki and S. Kitagawa, *Nat. Commun.*, 2019, **10**, 4362.
3 A. H. Assen, O. Yassine, O. Shekhah, M. Eddaoudi and K. N. Salama, *ACS Sens.*, 2017, **2**, 1294–1301.
4 Y. Quan, Y. Song, W. Shi, Z. Xu, J. S. Chen, X. Jiang, C. Wang and W. Lin, *J. Am. Chem. Soc.*, 2020, **142**, 8602–8607.
5 L. Feng, Y. Wang, S. Yuan, K.-Y. Wang, J.-L. Li, G. S. Day, D. Qiu, L. Cheng, W.-M. Chen, S. T. Madrahimov and H.-C. Zhou, *ACS Catal.*, 2019, **9**, 5111–5118.
6 M. D. Korzynski, D. F. Consoli, S. Zhang, Y. Roman-Leshkov and M. Dinca, *J. Am. Chem. Soc.*, 2018, **140**, 6956–6960.
7 P. M. Usov, B. Huffman, C. C. Epley, M. C. Kessinger, J. Zhu, W. A. Maza and A. J. Morris, *ACS Appl. Mater. Interfaces*, 2017, **9**, 33539–33543.
8 H. D. Park, M. Dinca and Y. Roman-Leshkov, *ACS Cent. Sci.*, 2017, **3**, 444–448.
9 L. Feng, K. Y. Wang, J. Willman and H. C. Zhou, *ACS Cent. Sci.*, 2020, **6**, 359–367.
10 J. E. Mondloch, W. Bury, D. Fairen-Jimenez, S. Kwon, E. J. DeMarco, M. H. Weston, A. A. Sarjeant, S. T. Nguyen, P. C. Stair, R. Q. Snurr, O. K. Farha and J. T. Hupp, *J. Am. Chem. Soc.*, 2013, **135**, 10294–10297.
11 D. Feng, Z. Y. Gu, J. R. Li, H. L. Jiang, Z. Wei and H. C. Zhou, *Angew. Chem., Int. Ed.*, 2012, **51**, 10307–10310.
12 J. Pang, S. Yuan, J. Qin, C. Liu, C. Lollar, M. Wu, D. Yuan, H. C. Zhou and M. Hong, *J. Am. Chem. Soc.*, 2017, **139**, 16939–16945.
13 W. Morris, B. Volosskiy, S. Demir, F. Gandara, P. L. McGrier, H. Furukawa, D. Cascio, J. F. Stoddart and O. M. Yaghi, *Inorg. Chem.*, 2012, **51**, 6443–6445.
14 X. Yu and S. M. Cohen, *J. Am. Chem. Soc.*, 2016, **138**, 12320–12323.
15 R. Limvorapitux, H. Chen, M. L. Mendonca, M. Liu, R. Q. Snurr and S. T. Nguyen, *Catal. Sci. Technol.*, 2019, **9**, 327–335.
16 J. Jiang, F. Gandara, Y. B. Zhang, K. Na, O. M. Yaghi and W. G. Klemperer, *J. Am. Chem. Soc.*, 2014, **136**, 12844–12847.
17 N. Van Velthoven, S. Waitschat, S. M. Chavan, P. Liu, S. Smolders, J. Vercammen, B. Bueken, S. Bals, K. P. Lillerud, N. Stock and D. E. De Vos, *Chem. Sci.*, 2019, **10**, 3616–3622.
18 H.-C. Zhou, T.-H. Yan, X.-L. Lv, K.-Y. Wang and L. Feng, *Natl. Sci. Rev.*, 2019, **7**, 1743–1758.
19 P. Deria, D. A. Gomez-Gualdron, I. Hod, R. Q. Snurr, J. T. Hupp and O. K. Farha, *J. Am. Chem. Soc.*, 2016, **138**, 14449–14457.
20 D. Feng, Z. Y. Gu, Y. P. Chen, J. Park, Z. Wei, Y. Sun, M. Bosch, S. Yuan and H. C. Zhou, *J. Am. Chem. Soc.*, 2014, **136**, 17714–17717.
21 D. Feng, W. C. Chung, Z. Wei, Z. Y. Gu, H. L. Jiang, Y. P. Chen, D. J. Darensbourg and H. C. Zhou, *J. Am. Chem. Soc.*, 2013, **135**, 17105–17110.
22 Q. Zhang, J. Su, D. Feng, Z. Wei, X. Zou and H. C. Zhou, *J. Am. Chem. Soc.*, 2015, **137**, 10064–10067.
23 T. Islamoglu, Z. Chen, M. C. Wasson, C. T. Buru, K. O. Kirlikovali, U. Afrin, M. R. Mian and O. K. Farha, *Chem. Rev.*, 2020, **120**, 8130–8160.
24 Z. Lu, J. Liu, X. Zhang, Y. Liao, R. Wang, K. Zhang, J. Lyu, O. K. Farha and J. T. Hupp, *J. Am. Chem. Soc.*, 2020, **142**, 21110–21121.
25 F. A. Son, M. C. Wasson, T. Islamoglu, Z. Chen, X. Gong, S. L. Hanna, J. Lyu, X. Wang, K. B. Idrees, J. J. Mahle, G. W. Peterson and O. K. Farha, *Chem. Mater.*, 2020, **32**, 4609–4617.
26 A. J. Young, R. Guillet-Nicolas, E. S. Marshall, F. Kleitz, A. J. Goodhand, L. B. L. Glanville, M. R. Reithofer and J. M. Chin, *Chem. Commun.*, 2019, **55**, 2190–2193.
27 J. E. Mondloch, M. J. Katz, W. C. Isley, 3rd, P. Ghosh, P. Liao, W. Bury, G. W. Wagner, M. G. Hall, J. B. DeCoste, G. W. Peterson, R. Q. Snurr, C. J. Cramer, J. T. Hupp and O. K. Farha, *Nat. Mater.*, 2015, **14**, 512–516.
28 M. J. Katz, J. E. Mondloch, R. K. Totten, J. K. Park, S. T. Nguyen, O. K. Farha and J. T. Hupp, *Angew. Chem., Int. Ed.*, 2014, **53**, 497–501.
29 K. Y. Cho, J. Y. Seo, H.-J. Kim, S. J. Pai, X. H. Do, H. G. Yoon, S. S. Hwang, S. S. Han and K.-Y. Baek, *Appl. Catal., B*, 2019, **245**, 635–647.
30 S. Y. Moon, Y. Liu, J. T. Hupp and O. K. Farha, *Angew. Chem., Int. Ed.*, 2015, **54**, 6795–6799.
31 B. J. Bucior, A. S. Rosen, M. Haranczyk, Z. Yao, M. E. Ziebel, O. K. Farha, J. T. Hupp, J. I. Siepmann, A. Aspuru-Guzik and R. Q. Snurr, *Cryst. Growth Des.*, 2019, **19**, 6682–6697.

